Impact of Virtual Admittance on Small-Signal Stability of Grid-Forming Inverters

Huang, Liang; Wu, Chao; Zhou, Dao; Blaabjerg, Frede

Published in:
Proceedings of the 2021 6th IEEE Workshop on the Electronic Grid (eGRID)

DOI (link to publication from Publisher):
10.1109/eGRID52793.2021.9662150

Publication date:
2021

Document Version
Accepted author manuscript, peer reviewed version

Impact of Virtual Admittance on Small-Signal Stability of Grid-Forming Inverters

Liang Huang*, Chao Wu+, Dao Zhou*, and Frede Blaabjerg*
*AAU Energy, Aalborg University, Aalborg East 9220, Denmark
+Department of Electrical Engineering, Shanghai Jiaotong University, Shanghai 200240, China
Email: lihu@energy.aau.dk, wuchao@sjtu.edu.cn, zda@energy.aau.dk, fbl@energy.aau.dk

***Abstract*—Conventional dual-loop grid-forming (GFM) inverters tend to be unstable when connecting to a stronger grid with a small grid inductance. Virtual inductance methods can increase the equivalent inductance to enhance stability. However, the impact of virtual inductance on the small-signal stability of GFM inverters is still absent in existing research. Hence, the stabilities of two virtual inductance methods (i.e. admittance method and impedance method) are compared initially in this paper. It is revealed that the stability range of the virtual admittance method is wider than that of the virtual impedance method. Besides, for the virtual admittance method, the stability is mainly influenced by the value of virtual admittance. A complex-value single-input single-output (SISO) small-signal model is proposed in this paper to find the critical stable value of the virtual admittance, which is not only simple but almost as accurate as the multiple-input multiple-output (MIMO) model. Finally, simulation results verify the effectiveness of theoretical analysis.**

Keywords—grid-forming inverter, small-signal stability, virtual admittance, single input single output method

I. Introduction

Nowadays, grid-following (GFL) inverters have been widely applied in renewable energy generation systems, such as wind and solar photovoltaic (PV) power plants. However, GFL inverters have some challenges to provide inertia support. Hence, the modern power system might suffer from frequency stability issues as the penetration of renewable energy sources increases and the total inertia decreases [1]. Additionally, GFL inverters behave like current sources, which rely on the grid voltage to realize synchronization and normal operation. Therefore, the islanded operation is also a big challenge for GFL inverters [2].

Differently, grid-forming (GFM) inverters can support the grid frequency to solve the frequency stability issues. Two commonly used methods are virtual synchronous generator (VSG) control and droop control methods to achieve the grid synchronization. When the virtual inertia is designed as zero, the VSG control method is equivalent to the droop control method [3]. In addition, GFM inverters behave like voltage sources so that they have the islanded operation ability. The islanded operation and frequency support are two obvious advantages of GFM inverters compared with GFL inverters. Therefore, GFM inverters have attracted a lot of attentions in recent years [4]-[9].

However, it is reported in [10] that conventional dual-loop GFM inverter is prone to be unstable under a stronger grid condition due to only a small grid inductance connecting two voltage sources on grid-side and converter-side. Hence, it is recommended in [10] to use another GFM control method without inner current loops. Because the total inductance between two voltage sources can be increased by including the filter inductance, the small-signal stability is able to be improved. However, the lack of current limitations and the poor voltage harmonic performance are two drawbacks of this method.

Similarly, an alternative idea is adding a virtual inductance to increase the total equivalent inductance between two voltage sources. To implement this idea, the virtual impedance method [11] and the virtual admittance method [12] are two interesting approaches. The equivalent circuits of these two methods are basically the same, but the stability ranges of them are different. Based on the eigenvalue analysis of these two methods, it is found that the small-signal stability range of the virtual admittance method is wider than that of the virtual impedance method. Therefore, the virtual admittance method is chosen for further study in this paper.

The value of the virtual admittance is determined by two parameters, namely the virtual resistance R_v and inductance X_v. It can also be represented by the magnitude and the phase angle (or the ratio of resistance and inductance R_v/X_v) in the complex-value form. This paper reveals that the magnitude of the virtual admittance and the ratio of the virtual resistance and inductance R_v/X_v are two key parameters to determine the small-signal stability of the GFM inverter system. The critical stable value of these two parameters can be found according to the eigenvalue analysis. Moreover, an equivalent complex-value single-input single-output (SISO) small-signal model is proposed in this paper, which allows to use Bode diagram to find the critical stable values. Compared with the multiple-input multiple-output (MIMO) model, this SISO model is not only simple but almost as accurate as the MIMO model. Thus, this SISO model can take place of the MIMO model for parameter design, which is convenient to use.

The rest of this paper is organized as follows. Section II introduces the configurations of three typical GFM inverter control schemes. Besides, their small-signal stabilities are also compared. In Section III, the impact of the virtual admittance on the small-signal stability is analyzed. Besides, an SISO method is introduced to find the critical values. In Section IV, simulation results are provided to verify the theoretical analysis. Finally, this paper is concluded in Section V.

II. Stability Comparison of Three Grid-Forming Control Methods

A. Configurations of Three Grid-Forming Control Schemes

Three typical GFM control methods and equivalent circuits are presented in Fig. 1, where G_v and G_i are the closed-loop transfer functions of the voltage control loop and current control loop. L_f and C_f are the filter inductance and capacitance. L_g and v_g are the grid inductance and grid voltage of Thevenin's equivalent circuit of the power grid.

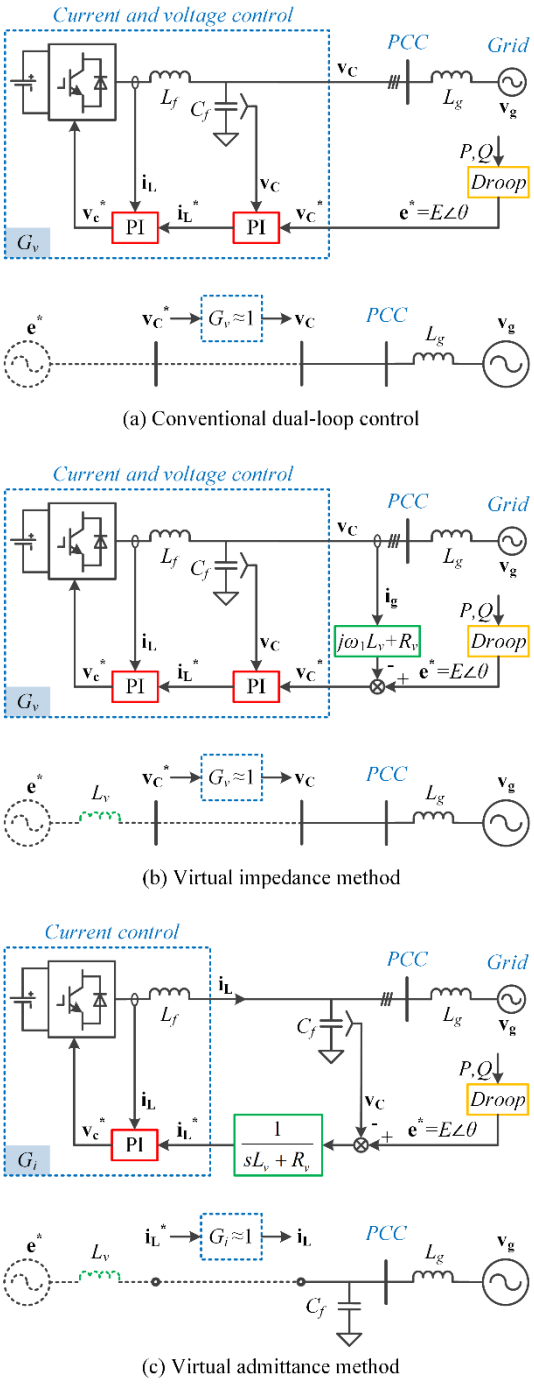

(a) Conventional dual-loop control

(b) Virtual impedance method

(c) Virtual admittance method

Fig. 1. Three typical grid-forming control methods and equivalent circuits.

The conventional dual-loop GFM inverter with droop control is shown in Fig. 1(a), which is the same as [13]. The virtual impedance method is shown in Fig. 1(b), where a virtual impedance $Z_v = R_v + j\omega_1 L_v$ is directly added based on the conventional dual-loop control method. Fig. 1(c) demonstrates an alternative method by adding a virtual admittance $Y_v = 1/(sL_v + R_v)$. Their equivalent circuits are also shown in Fig. 1. Intuitively, both the virtual impedance method and the virtual admittance method can increase the equivalent inductance between two voltage sources to enhance the stability of the conventional dual-loop control method. However, a quantitative comparison regarding stability is still absent in existing research. Hence, small-signal stabilities of these three methods will be compared quantitatively in this section.

B. Small-Signal State-Space Models and Stability Analysis

The detailed control structure of the conventional dual-loop GFM control method can be seen in [13], which is not given in this paper. The small-signal differential equations of each method shown in Fig. 1 will be derived in this section. Same as [13], the superscript '^{ctrl}' denotes the variables in the control d-q frame in this paper. Besides, the subscript '$_0$' denotes a steady-state operating point, and the symbol 'Δ' denotes a small-signal perturbation of a variable.

The small-signal differential equations of the L_f- C_f- L_g circuits in the system d-q frame are given by (1)-(3).

$$\begin{cases} \Delta v_{Cd} - \Delta v_{gd} = L_g \dfrac{d\Delta i_{gd}}{dt} + R_g \Delta i_{gd} - \omega_1 L_g \Delta i_{gq} \\ \Delta v_{Cq} - \Delta v_{gq} = L_g \dfrac{d\Delta i_{gq}}{dt} + R_g \Delta i_{gq} + \omega_1 L_g \Delta i_{gd} \end{cases} \tag{1}$$

$$\begin{cases} \Delta i_{Ld} - \Delta i_{gd} = C_f \dfrac{d\Delta v_{Cd}}{dt} - \omega_1 C_f \Delta v_{Cq} \\ \Delta i_{Lq} - \Delta i_{gq} = C_f \dfrac{d\Delta v_{Cq}}{dt} + \omega_1 C_f \Delta v_{Cd} \end{cases} \tag{2}$$

$$\begin{cases} \Delta v_{cd}^{\ *} - \Delta v_{Cd} = L_f \dfrac{d\Delta i_{Ld}}{dt} + R_f \Delta i_{Ld} - \omega_1 L_f \Delta i_{Lq} \\ \Delta v_{cq}^{\ *} - \Delta v_{Cq} = L_f \dfrac{d\Delta i_{Lq}}{dt} + R_f \Delta i_{Lq} + \omega_1 L_f \Delta i_{Ld} \end{cases} \tag{3}$$

According to the Park and iPark transformations, the small-signal equations of the coordinate transformations can be derived as (4)-(7), where $\Delta\theta_{ps}$ is the angle between the control d-q frame and the grid d-q frame [13].

$$\begin{cases} \Delta v_{Cd}^{\ ctrl} = \Delta v_{Cd} + v_{Cq0} \cdot \Delta\theta_{ps} \\ \Delta v_{Cq}^{\ ctrl} = \Delta v_{Cq} - v_{Cd0} \cdot \Delta\theta_{ps} \end{cases} \tag{4}$$

$$\begin{cases} \Delta i_{gd}^{\ ctrl} = \Delta i_{gd} + i_{gq0} \cdot \Delta\theta_{ps} \\ \Delta i_{gq}^{\ ctrl} = \Delta i_{gq} - i_{gd0} \cdot \Delta\theta_{ps} \end{cases} \tag{5}$$

$$\begin{cases} \Delta i_{Ld}^{\ ctrl} = \Delta i_{Ld} + i_{Lq0} \cdot \Delta\theta_{ps} \\ \Delta i_{Lq}^{\ ctrl} = \Delta i_{Lq} - i_{Ld0} \cdot \Delta\theta_{ps} \end{cases} \tag{6}$$

$$\begin{cases} \Delta v_{cd}^{\ *} = \Delta v_{cd}^{\ *ctrl} - v_{cq0} \cdot \Delta\theta_{ps} \\ \Delta v_{cq}^{\ *} = \Delta v_{cq}^{\ *ctrl} + v_{cd0} \cdot \Delta\theta_{ps} \end{cases} \tag{7}$$

Besides, the small-signal linearized equations of the current control loops are provided by (8) and (9).

$$\begin{cases} \dfrac{d\Delta Int_{id}}{dt} = \Delta i_{Ld}^{\ *} - \Delta i_{Ld}^{\ ctrl} \\ \Delta v_{cd}^{\ *ctrl} = K_{p\_id}(\Delta i_{Ld}^{\ *} - \Delta i_{Ld}^{\ ctrl}) + K_{i\_id}\Delta Int_{id} - \omega_1 L_f \Delta i_{Lq}^{\ ctrl} \end{cases} \tag{8}$$

$$\begin{cases} \dfrac{d\Delta Int_{iq}}{dt} = \Delta i_{Lq}^{\ *} - \Delta i_{Lq}^{\ ctrl} \\ \Delta v_{cq}^{\ *ctrl} = K_{p\_iq}(\Delta i_{Lq}^{\ *} - \Delta i_{Lq}^{\ ctrl}) + K_{i\_iq}\Delta Int_{iq} + \omega_1 L_f \Delta i_{Ld}^{\ ctrl} \end{cases} \tag{9}$$

Moreover, the small-signal linearized equations of the voltage control loops are given by (10) and (11).

$$\begin{cases} \dfrac{d\Delta Int_{vd}}{dt} = \Delta v_{Cd}^{\ *} - \Delta v_{Cd}^{\ ctrl} \\ \Delta i_{Ld}^{\ *} = K_{p\_vd}(\Delta v_{Cd}^{\ *} - \Delta v_{Cd}^{\ ctrl}) + K_{i\_vd}\Delta Int_{vd} - \omega_1 C_f \Delta v_{Cq}^{\ ctrl} \end{cases} \tag{10}$$

$$\begin{cases} \dfrac{d\Delta Int_{vq}}{dt} = \Delta v_{Cq}^{\ *} - \Delta v_{Cq}^{\ ctrl} \\ \Delta i_{Lq}^{\ *} = K_{p\_vq}(\Delta v_{Cq}^{\ *} - \Delta v_{Cq}^{\ ctrl}) + K_{i\_vq}\Delta Int_{vq} + \omega_1 C_f \Delta v_{Cd}^{\ ctrl} \end{cases} \tag{11}$$

In addition, the small-signal linearized equations of the active power and reactive power can be derived as (12)-(13).

$$\Delta P^{ctrl} = \frac{3}{2}\begin{bmatrix} i_{gd0} & i_{gq0} \end{bmatrix} \cdot \begin{bmatrix} \Delta v_{Cd}^{\ ctrl} \\ \Delta v_{Cq}^{\ ctrl} \end{bmatrix} + \frac{3}{2}\begin{bmatrix} v_{Cd0} & v_{Cq0} \end{bmatrix} \cdot \begin{bmatrix} \Delta i_{gd}^{\ ctrl} \\ \Delta i_{gq}^{\ ctrl} \end{bmatrix} \tag{12}$$

$$\Delta Q^{ctrl} = \frac{3}{2}\begin{bmatrix} -i_{gq0} & i_{gd0} \end{bmatrix} \begin{bmatrix} \Delta v_{Cd}^{\ ctrl} \\ \Delta v_{Cq}^{\ ctrl} \end{bmatrix} + \frac{3}{2}\begin{bmatrix} v_{Cq0} & -v_{Cd0} \end{bmatrix} \begin{bmatrix} \Delta i_{gd}^{\ ctrl} \\ \Delta i_{gq}^{\ ctrl} \end{bmatrix} \tag{13}$$

The small-signal differential equations of the first-order low-pass filter (LPF) are given by (14).

$$\begin{cases} \dfrac{d\Delta P^{ctrl}_{\ \ LPF}}{dt} + \omega_{LPF}\Delta P^{ctrl}_{\ \ LPF} = \omega_{LPF}\Delta P^{ctrl} \\ \dfrac{d\Delta Q^{ctrl}_{\ \ LPF}}{dt} + \omega_{LPF}\Delta Q^{ctrl}_{\ \ LPF} = \omega_{LPF}\Delta Q^{ctrl} \end{cases} \tag{14}$$

where ω_{LPF} is the cut-off angular frequency of the LPFs.

Furthermore, the small-signal equations of the P-droop and Q-droop control are presented by (15).

$$\begin{cases} \dfrac{d\Delta\theta_{ps}}{dt} = \Delta\omega_{ps} = m_p(\Delta P^* - \Delta P^{ctrl}_{\ \ LPF}) \\ \Delta E = n_q(\Delta Q^* - \Delta Q^{ctrl}_{\ \ LPF}) \end{cases} \tag{15}$$

For the conventional dual-loop GFM control method, the reference values of the voltage control loop are shown in (16).

$$\begin{cases} \Delta v_{Cd}^{\ *} = \Delta E \\ \Delta v_{Cq}^{\ *} = 0 \end{cases} \tag{16}$$

According to (1)-(16), the small-signal state-space model of conventional dual-loop GFM control can be derived as:

$$\mathbf{\Delta\dot{x}_{1(13\times1)}} = \mathbf{A_{1(13\times13)}} \cdot \mathbf{\Delta x_{1(13\times1)}} + \mathbf{B_{1(13\times4)}} \cdot \mathbf{\Delta u_{1(4\times1)}} \tag{17}$$

where $\mathbf{\Delta x_{1(13\times1)}} = [\Delta i_{gd}, \Delta i_{gq}, \Delta v_{Cd}, \Delta v_{Cq}, \Delta i_{Ld}, \Delta i_{Lq}, \Delta Int_{id}, \Delta Int_{iq}, \Delta int_{vd}, \Delta int_{vq}, \Delta P_{LPF}^{\ ctrl}, \Delta\theta_{ps}, \Delta Q_{LPF}^{\ ctrl}]^{\mathrm{T}}$ and $\mathbf{\Delta u_{1(4\times1)}} = [\Delta v_{gd}, \Delta v_{gq}, \Delta P^*, \Delta Q^*]$.

For the virtual impedance method in Fig. 1(b), the reference values of the voltage control loop are shown in (18).

$$\begin{cases} \Delta v_{Cd}^{\ *} = \Delta E - R_v\Delta i_{Ld}^{\ ctrl} + \omega_1 L_v \Delta i_{Lq}^{\ ctrl} \\ \Delta v_{Cq}^{\ *} = 0 - R_v\Delta i_{Lq}^{\ ctrl} - \omega_1 L_v \Delta i_{Ld}^{\ ctrl} \end{cases} \tag{18}$$

Similarly, according to (1)-(15) and (18), the small-signal state-space model of the virtual impedance method can be derived as (19).

TABLE I. PARAMETERS OF GRID-FORMING INVERTER

Parameters	Values
Grid phase voltage V_g and nomimal voltage V_N	$V_N = V_g$ =311 V
Grid frequency f_g and nomimal frequency ω_N	$\omega_N = 2\pi f_g = 2\pi\cdot 50$ Hz
Rated power of inverter S_N and P_N	$P_N = S_N$ =30 kVA
Maximum current of inverter (peak value), I_{max}	64.3 A
DC-link voltage, V_{dc}	700 V
Output filter inductor, L_f	5 mH
Output filter capacitor, C_f	10 μF
R/X ratio of grid impedance, R_g/X_g	0.01
Short circuit ratio, SCR	1~30
Grid inductor, L_g	0.5~15.3 mH
Grid resistor, R_g	1.6~48 mΩ
Switching/sampling frequency, f_s	10 kHz
Designed current-loop bandwidth, ω_i	2000 rad/s
Designed voltage-loop bandwidth, ω_v	400 rad/s
Active power droop coefficient, m_p	2.5% ω_N/P_N
Reactive power droop coefficient, n_q	2.5% V_N/P_N
Cut-off angular frequency of LPF, ω_{LPF}	300 rad/s
Virtual impedance $Z_v = \lvert Z_v\rvert\angle\arctan(X_v/R_v)$	$\lvert Z_v\rvert$ = 0.5 pu, and R_v/X_v = 0.1
Virtual admittance $Y_v = [\lvert Z_v\rvert\angle\arctan(X_v/R_v)]^{-1}$	$\lvert Z_v\rvert$ = 0.5 pu, and R_v/X_v = 0.1

$$\mathbf{\Delta\dot{x}_{2(13\times1)}} = \mathbf{A_{2(13\times13)}} \cdot \mathbf{\Delta x_{2(13\times1)}} + \mathbf{B_{2(13\times4)}} \cdot \mathbf{\Delta u_{2(4\times1)}} \tag{19}$$

where $\mathbf{\Delta x_{2(13\times1)}} = \mathbf{\Delta x_{1(13\times1)}}$ and $\mathbf{\Delta u_{2(4\times1)}} = \mathbf{\Delta u_{1(4\times1)}}$.

For the virtual admittance method in Fig. 1(c), the small-signal equations of current reference values are shown in (20).

$$\begin{cases} L_v \dfrac{d\Delta i_{Ld}^{\ *}}{dt} + R_v\Delta i_{Ld}^{\ *} - \omega_1 L_v \Delta i_{Lq}^{\ *} = \Delta E - \Delta v_{Cd}^{\ ctrl} \\ L_v \dfrac{d\Delta i_{Lq}^{\ *}}{dt} + R_v\Delta i_{Lq}^{\ *} + \omega_1 L_v \Delta i_{Ld}^{\ *} = 0 - \Delta v_{Cq}^{\ ctrl} \end{cases} \tag{20}$$

According to (1)-(9), (12)-(15), and (20), the state-space model of the virtual admittance method can be derived as (21).

$$\mathbf{\Delta\dot{x}_{3(13\times1)}} = \mathbf{A_{3(13\times13)}} \cdot \mathbf{\Delta x_{3(13\times1)}} + \mathbf{B_{3(13\times4)}} \cdot \mathbf{\Delta u_{3(4\times1)}} \tag{21}$$

where $\mathbf{\Delta x_{3(13\times1)}} = [\Delta i_{gd}, \Delta i_{gq}, \Delta v_{Cd}, \Delta v_{Cq}, \Delta i_{Ld}, \Delta i_{Lq}, \Delta Int_{id}, \Delta Int_{iq}, \Delta i_{Ld}^{\ *}, \Delta i_{Lq}^{\ *}, \Delta P_{LPF}^{\ ctrl}, \Delta\theta_{ps}, \Delta Q_{LPF}^{\ ctrl}]^{\mathrm{T}}$ and $\mathbf{\Delta u_{3(4\times1)}} = \mathbf{\Delta u_{1(4\times1)}}$.

Considering the stability depends on $\mathbf{A}$, only the matrixes $\mathbf{A_{1(13\times13)}}$, $\mathbf{A_{2(13\times13)}}$ and $\mathbf{A_{3(13\times13)}}$ are given in Appendix. Since the power has weak impact on the small-signal stability, the zero power condition is used for analysis in this paper. Thus, the calculation of steady-state operating points is same as [13].

The system and control parameters of a 30 kW GFM inverter are shown in Table I. The grid strength can be described by the short circuit ratio (SCR) [14]. Based on matrixes $\mathbf{A_{1(13\times13)}}$, $\mathbf{A_{2(13\times13)}}$ and $\mathbf{A_{3(13\times13)}}$ in (17), (19), and (21), the dominant eigenvalues near the imaginary axis of three state-space models are presented in Fig. 2, where the SCR is changed to evaluate the stability under different grid strengths.

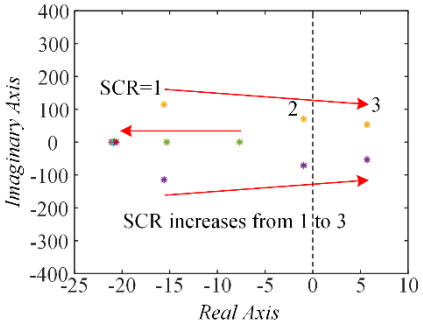

(a) Conventional dual-loop control

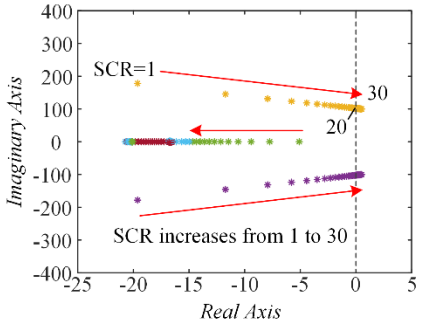

(b) Virtual impedance method

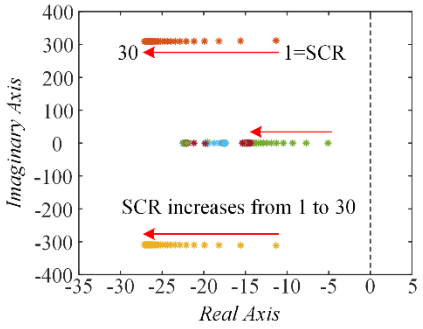

(c) Virtual admittance method

Fig. 2. Dominant eigenvalues of small-signal state-space models of three grid-forming control methods with different SCRs.

Fig. 2(a) shows eigenvalues of the conventional dual-loop control method. When the SCR is increased to 3, the system becomes unstable. Fig. 2(b) shows eigenvalues of the virtual impedance method. When the SCR is increased to 20, it becomes unstable. Besides, Fig. 2(c) shows eigenvalues of the virtual admittance method. As the SCR increases, the eigenvalues move to left (far from the right half plane). Thus, the stability range regarding the SCR can be considered as [1, ∞]. Therefore, the stability range of the virtual admittance method is larger than that of the other two methods. Due to this advantage, the virtual admittance method will be the focus in this paper. Notably, the case SCR<1 is not considered in this paper because SCR=1 is the benchmark weak grid [15].

III. Stability Analysis of Virtual Admittance Based Grid-Forming Inverter

For the virtual admittance based GFM inverter, the small-signal stability is mainly influenced by the value of virtual admittance. The eigenvalues of small-signal state-space models with different $|Z_v|$ and R_v/X_v are shown in Fig. 3 and Fig. 4 respectively. It can be seen that $|Z_v|$ = 0.4 pu and R_v/X_v = 1.1 are the critical stable points.

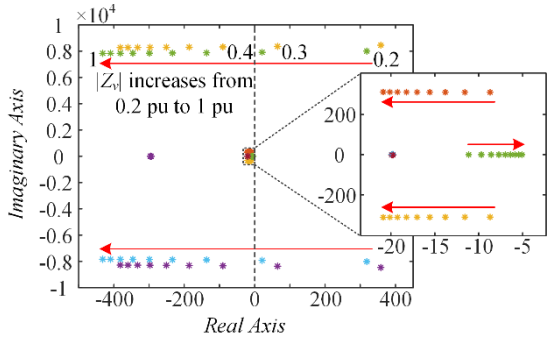

(a) Grid-connected mode

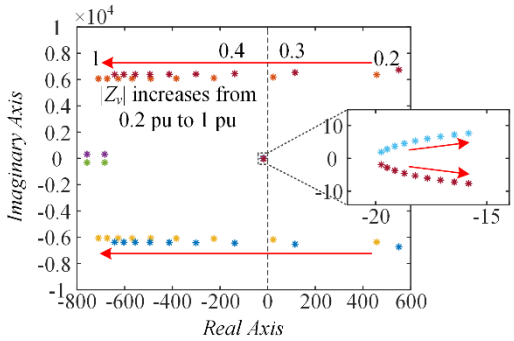

(b) Initial start-up mode without grid connection

Fig. 3. Eigenvalues of small-signal state-space models of virtual admittance method with different $|Z_v|$ when SCR is 2.

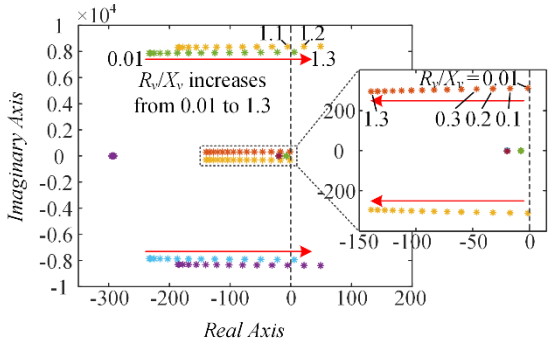

(a) Grid-connected mode

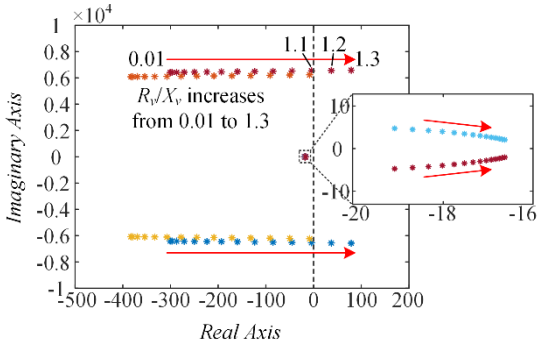

(b) Initial start-up mode without grid connection

Fig. 4. Eigenvalues of small-signal state-space models of virtual admittance method with different R_v/X_v when SCR is 2.

Besides, the eigenvalues of the grid-connected mode and the initial start-up mode without grid-connection are compared in Fig. 3 and Fig. 4. It can be seen that the critical stable values of $|Z_v|$ and R_v/X_v in these two operating modes are basically the same.

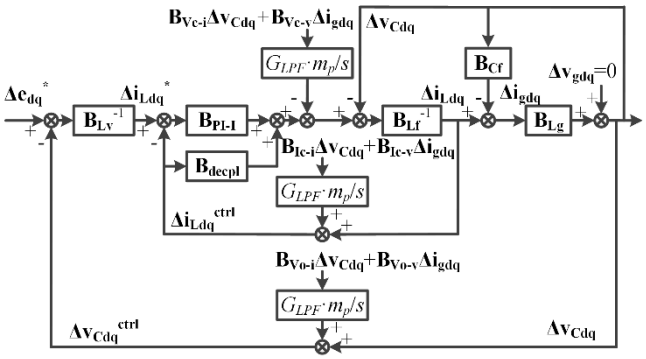

(a) Grid-connected mode

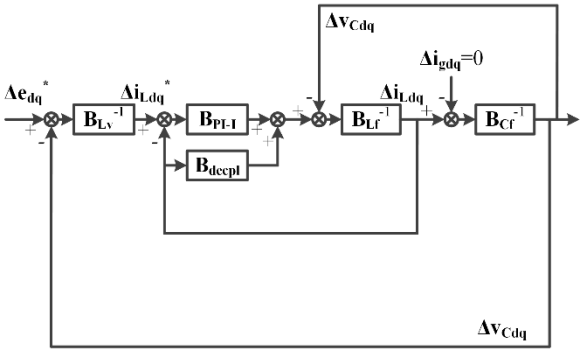

(b) Initial start-up mode without grid-connection

Fig. 5. Small-signal control structures of virtual admittance method in two operating modes.

Based on the eigenvalue analysis results in Fig. 3 and Fig. 4, the small-signal models of the virtual admittance method in the grid-connected mode and the initial start-up mode basically have the same critical values to determine the stability. Thus, the small-signal model of the initial start-up mode is preferable to be used for stability analysis and finding the critical stable points, because it is simpler.

Since the time-domain small-signal model and the frequency-domain small-signal model can be derived from each other [16], the time-domain state-space model of the virtual admittance method in (21) can also be represented by the frequency-domain model shown in Fig. 5(a), where the 2×2 matrixes $\mathbf{B}_{PI\text{-}I}$, $\mathbf{B}_{Lf}$, $\mathbf{B}_{Cf}$, etc are the same as [13]. Thus, in the initial start-up mode without grid-connection, the small-signal model can be simplified as Fig. 5(b).

According to the frequency-domain small-signal model in Fig. 5(b), the open-loop transfer function matrix from $\Delta\mathbf{e}_{dq}^{*}$ to $\Delta\mathbf{v}_{Cdq}$ can be derived as (22).

$$\mathbf{T}_{ol}(s)=\mathbf{B}_{Lv}^{-1}\cdot[(\mathbf{B}_{Lf}+\mathbf{B}_{PI\text{-}I}-\mathbf{B}_{decpl})\mathbf{B}_{Cf}+\mathbf{I}]^{-1}\cdot\mathbf{B}_{PI\text{-}I} \quad (22)$$

Since all the matrixes in (22) are symmetric, they can be represented by the complex vector form, as shown in (23).

$$T_{ol}(s)=\frac{\dfrac{1}{sL_v+R_v+j\omega_1 L_v}\cdot\left(K_{p\_idq}+\dfrac{K_{i\_idq}}{s}\right)}{(sL_f+R_f+K_{p\_idq}+\dfrac{K_{i\_idq}}{s})(sC_f+j\omega_1 C_f)+1} \quad (23)$$

According to the open-loop transfer function $T_{ol}(s)$ in (23), the SISO method can be used for stability analysis. The Bode diagrams of $T_{ol}(s)$ are shown in Fig. 6.

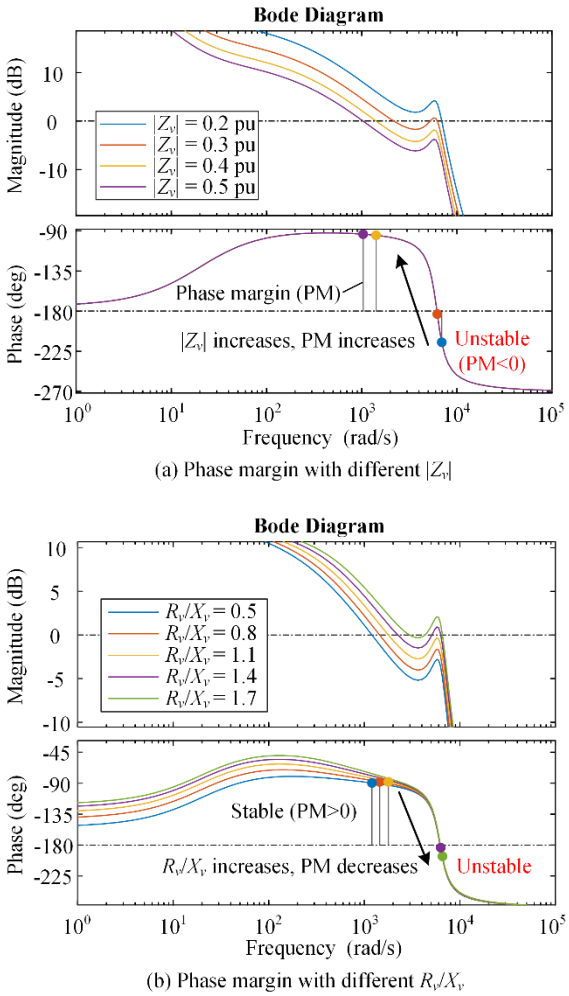

(a) Phase margin with different $|Z_v|$

(b) Phase margin with different R_v/X_v

Fig. 6. Bode diagrams of open-loop transfer function $T_{ol}(s)$.

It can be seen in Fig. 6(a) that the system is unstable when $|Z_v|$ is smaller than 0.4 pu, while it is stable when $|Z_v|$ is larger than 0.4 pu. Thus, 0.4 pu can be considered as the critical stable value for $|Z_v|$. Similarly, according to the stability analysis results in Fig. 6(b), the ratio 1.1 can be considered as the critical stable value for R_v/X_v. The stability analysis results in Fig. 6 agree with that in Fig. 3 and Fig. 4. Thus, it is easy to use this SISO method to design the parameters $|Z_v|$ and R_v/X_v according to the phase margin requirement (e.g. ≥ 45 degree).

IV. Simulation Results

In order to verify the correctness of the analyses above, a 30 kW virtual admittance based GFM inverter simulation model is established in Matlab/Simulink. The system and control parameters are shown in Table I, which are the same as the parameters used for stability analyses. To avoid the influence of the high-frequency harmonics, an average model of the inverter is used. A weak grid condition with SCR = 1 and a strong grid condition with SCR = 30 are used as examples to evaluate the stability of the virtual admittance control method. The simulation results with different $|Z_v|$ and R_v/X_v are shown in Fig. 7 and Fig. 8 respectively.

It can be seen from Fig. 7 that the system is stable initially, but when the parameter $|Z_v|$ is reduced from 0.5 pu to 0.3 pu at the moment of 3.5s, the system becomes unstable. Then, when $|Z_v|$ is increased to 0.5 pu at the instant of 5s, the system becomes stable again. These simulation results reflect that a larger $|Z_v|$ is beneficial for the small-signal stability.

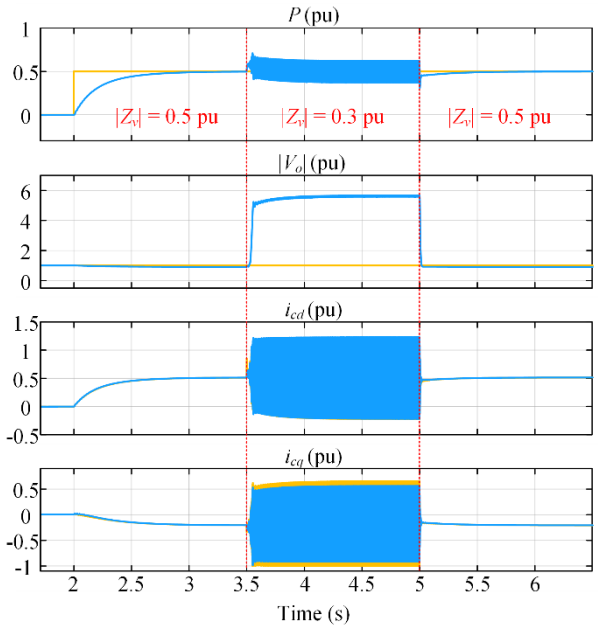

(a) Weak grid condition (SCR=1)

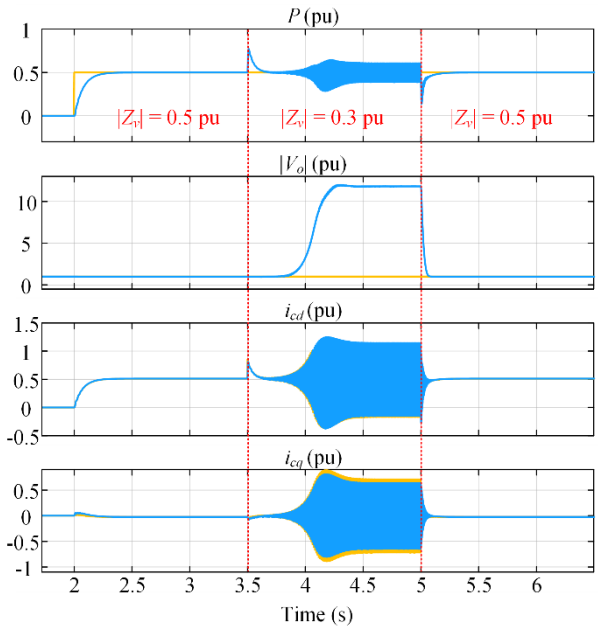

(b) Strong grid condition (SCR=30)

Fig. 7. Simulation results of virtual admittance method with different $|Z_v|$.

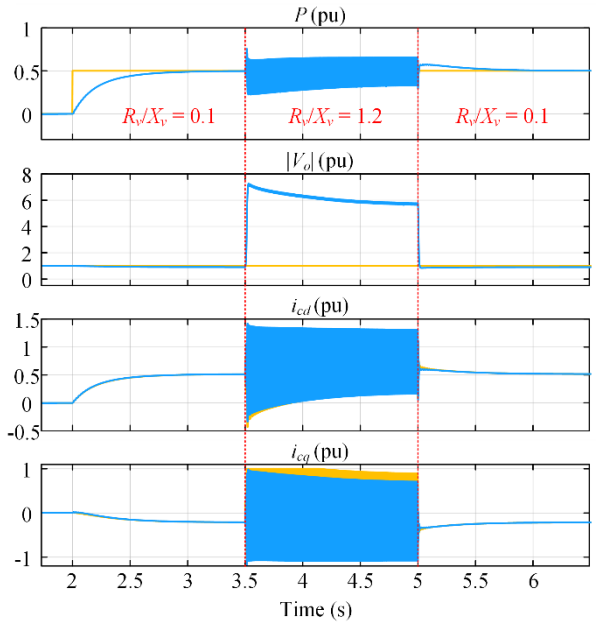

(a) Weak grid condition (SCR=1)

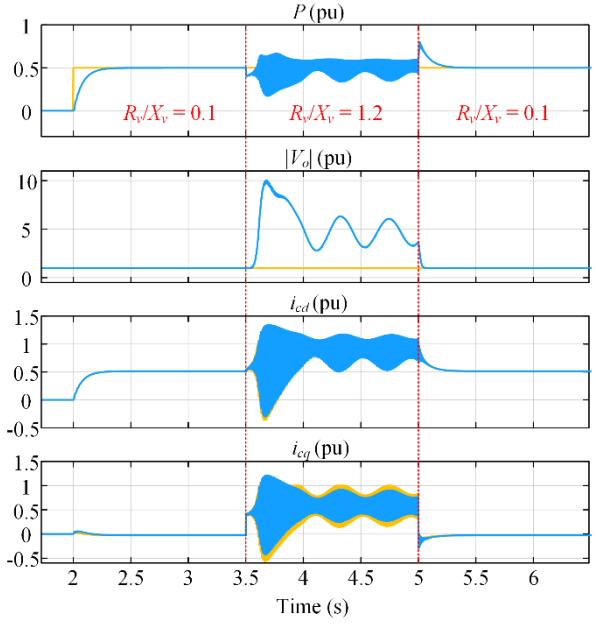

(b) Strong grid condition (SCR=30)

Fig. 8. Simulation results of virtual admittance method with different R_v/X_v.

Moreover, it can be seen from Fig. 8 that when the parameter R_v/X_v is increased from 0.1 to 1.2 at the moment of 3.5s, the system becomes unstable. However, when R_v/X_v is decreased to 0.1 at the instant of 5s, the system becomes stable again. These simulation results reflect that a smaller R_v/X_v is beneficial for stability. The same stability feature can be observed under weak grid and strong grid conditions, which means the robustness of the virtual admittance method is quite good if the value of virtual admittance Y_v is designed properly. The simulation results in Fig. 7 and Fig. 8 agree well with the stability analysis results in Fig. 6(a) and Fig. 6(b).

Furthermore, it is worth mentioning that although a smaller R_v/X_v is beneficial for stability, the purely inductive case $R_v/X_v = 0$ should be avoided. Because if R_v/X_v is close to 0, the synchronous oscillation will appear. Thus, the R_v/X_v equal to 0.1 or 0.2 is recommended to use.

V. Conclusion

This paper reveals that both the virtual impedance method and the virtual admittance method can enhance the stability of the conventional dual-loop GFM inverter. Besides, the virtual admittance method has wider stability ranges than the virtual impedance method regarding the SCR, so the virtual admittance method is preferable to be used in this paper. It is revealed that the magnitude $|Z_v|$ and the ratio R_v/X_v are two key parameters to determine the stability of the virtual admittance method. Moreover, a simple SISO stability analysis method is proposed in this paper to find the critical stable points. The accuracy of this SISO method is basically same as the eigenvalue analysis results of the MIMO state-space model. Thus, it is simpler to use this SISO method for parameter design. When the virtual admittance is designed properly, the inverter is stable no matter the grid is strong or weak.

APPENDIX

$\mathbf{A}_{1(13\times13)}$ =

$$\begin{bmatrix}
\frac{-R_g}{L_g} & \omega_1 & \frac{1}{L_g} & 0 & 0 & 0 & 0 & 0 & 0 & 0 & 0 & 0 & 0 \\
-\omega_1 & \frac{-R_g}{L_g} & 0 & \frac{1}{L_g} & 0 & 0 & 0 & 0 & 0 & 0 & 0 & 0 & 0 \\
\frac{-1}{C_f} & 0 & 0 & \omega_1 & \frac{1}{C_f} & 0 & 0 & 0 & 0 & 0 & 0 & 0 & 0 \\
0 & \frac{-1}{C_f} & -\omega_1 & 0 & 0 & \frac{1}{C_f} & 0 & 0 & 0 & 0 & 0 & 0 & 0 \\
0 & 0 & \frac{1+K_{p_id}K_{p_vd}}{-L_f} & \frac{K_{p_id}\omega_1 C_f}{-L_f} & \frac{R_f+K_{p_id}}{-L_f} & 0 & \frac{K_{i_id}}{L_f} & 0 & \frac{K_{p_id}K_{i_vd}}{L_f} & 0 & 0 & A_{1(12,5)} & \frac{K_{p_id}K_{p_vd}n_q}{-L_f} \\
0 & 0 & \frac{K_{p_iq}\omega_1 C_f}{L_f} & \frac{1+K_{p_iq}K_{p_vq}}{-L_f} & 0 & \frac{R_f+K_{p_iq}}{-L_f} & 0 & \frac{K_{i_iq}}{L_f} & 0 & \frac{K_{p_iq}K_{i_vq}}{L_f} & 0 & A_{1(12,6)} & 0 \\
0 & 0 & -K_{p_vd} & -\omega_1 C_f & -1 & 0 & 0 & 0 & K_{i_vd} & 0 & 0 & A_{1(12,7)} & -K_{p_vd}n_q \\
0 & 0 & \omega_1 C_f & -K_{p_vq} & 0 & -1 & 0 & 0 & 0 & K_{i_vq} & 0 & A_{1(12,8)} & 0 \\
0 & 0 & -1 & 0 & 0 & 0 & 0 & 0 & 0 & 0 & 0 & -v_{Cq0} & -n_q \\
0 & 0 & 0 & -1 & 0 & 0 & 0 & 0 & 0 & 0 & 0 & v_{Cd0} & 0 \\
\frac{3}{2}\omega_{LPF}v_{Cd0} & \frac{3}{2}\omega_{LPF}v_{Cq0} & \frac{3}{2}\omega_{LPF}i_{gd0} & \frac{3}{2}\omega_{LPF}i_{gq0} & 0 & 0 & 0 & 0 & 0 & 0 & -\omega_{LPF} & 0 & 0 \\
0 & 0 & 0 & 0 & 0 & 0 & 0 & 0 & 0 & 0 & -m_p & 0 & 0 \\
\frac{3}{2}\omega_{LPF}v_{Cq0} & \frac{-3}{2}\omega_{LPF}v_{Cd0} & \frac{-3}{2}\omega_{LPF}i_{gq0} & \frac{3}{2}\omega_{LPF}i_{gd0} & 0 & 0 & 0 & 0 & 0 & 0 & 0 & 0 & -\omega_{LPF}
\end{bmatrix} \tag{A1}$$

where $A_{1(12,5)} = (\omega_1 L_f i_{Ld0} - v_{cq0})/L_f + K_{p\_id}(-K_{p\_vd}v_{Cq0} + \omega_1 C_f v_{Cd0} - i_{Lq0})/L_f$, $A_{1(12,6)} = (\omega_1 L_f i_{Lq0} + v_{cd0})/L_f + K_{p\_iq}(K_{p\_vq}v_{Cd0} + \omega_1 C_f v_{Cq0} + i_{Ld0})/L_f$, $A_{1(12,7)} = -K_{p\_vd}v_{Cq0} + \omega_1 C_f v_{Cd0} - i_{Lq0}$, and $A_{1(12,8)} = K_{p\_vq}v_{Cd0} + \omega_1 C_f v_{Cq0} + i_{Ld0}$.

$\mathbf{A}_{2(13\times13)}$ =

$$\begin{bmatrix}
\frac{-R_g}{L_g} & \omega_1 & \frac{1}{L_g} & 0 & 0 & 0 & 0 & 0 & 0 & 0 & 0 & 0 & 0 \\
-\omega_1 & \frac{-R_g}{L_g} & 0 & \frac{1}{L_g} & 0 & 0 & 0 & 0 & 0 & 0 & 0 & 0 & 0 \\
\frac{-1}{C_f} & 0 & 0 & \omega_1 & \frac{1}{C_f} & 0 & 0 & 0 & 0 & 0 & 0 & 0 & 0 \\
0 & \frac{-1}{C_f} & -\omega_1 & 0 & 0 & \frac{1}{C_f} & 0 & 0 & 0 & 0 & 0 & 0 & 0 \\
0 & 0 & \frac{1+K_{p_id}K_{p_vd}}{-L_f} & \frac{K_{p_id}\omega_1 C_f}{-L_f} & A_{2(5,5)} & A_{2(5,6)} & \frac{K_{i_id}}{L_f} & 0 & \frac{K_{p_id}K_{i_vd}}{L_f} & 0 & 0 & A_{2(12,5)} & \frac{K_{p_id}K_{p_vd}n_q}{-L_f} \\
0 & 0 & \frac{K_{p_iq}\omega_1 C_f}{L_f} & \frac{1+K_{p_iq}K_{p_vq}}{-L_f} & A_{2(6,5)} & A_{2(6,6)} & 0 & \frac{K_{i_iq}}{L_f} & 0 & \frac{K_{p_iq}K_{i_vq}}{L_f} & 0 & A_{2(12,6)} & 0 \\
0 & 0 & -K_{p_vd} & -\omega_1 C_f & -1-K_{p_vd}R_v & K_{p_vd}\omega_1 L_v & 0 & 0 & K_{i_vd} & 0 & 0 & A_{2(12,7)} & -K_{p_vd}n_q \\
0 & 0 & \omega_1 C_f & -K_{p_vq} & -K_{p_vq}\omega_1 L_v & -1-K_{p_vq}R_v & 0 & 0 & 0 & K_{i_vq} & 0 & A_{2(12,8)} & 0 \\
0 & 0 & -1 & 0 & -R_v & \omega_1 L_v & 0 & 0 & 0 & 0 & 0 & A_{2(12,9)} & -n_q \\
0 & 0 & 0 & -1 & -\omega_1 L_v & -R_v & 0 & 0 & 0 & 0 & 0 & A_{2(12,10)} & 0 \\
\frac{3}{2}\omega_{LPF}v_{Cd0} & \frac{3}{2}\omega_{LPF}v_{Cq0} & \frac{3}{2}\omega_{LPF}i_{gd0} & \frac{3}{2}\omega_{LPF}i_{gq0} & 0 & 0 & 0 & 0 & 0 & 0 & -\omega_{LPF} & 0 & 0 \\
0 & 0 & 0 & 0 & 0 & 0 & 0 & 0 & 0 & 0 & -m_p & 0 & 0 \\
\frac{3}{2}\omega_{LPF}v_{Cq0} & \frac{-3}{2}\omega_{LPF}v_{Cd0} & \frac{-3}{2}\omega_{LPF}i_{gq0} & \frac{3}{2}\omega_{LPF}i_{gd0} & 0 & 0 & 0 & 0 & 0 & 0 & 0 & 0 & -\omega_{LPF}
\end{bmatrix} \tag{A2}$$

where $A_{2(5,5)} = -R_f/L_f - K_{p\_id}(1+K_{p\_vd}R_v)/L_f$, $A_{2(5,6)} = K_{p\_id}K_{p\_vd}\,\omega_1 L_v/L_f$, $A_{2(6,5)} = -K_{p\_iq}K_{p\_vq}\,\omega_1 L_v/L_f$, $A_{2(6,6)} = -R_f/L_f - K_{p\_iq}(1+K_{p\_vq}R_v)/L_f$, $A_{2(12,5)} = (\omega_1 L_f i_{Ld0} - v_{cq0})/L_f + K_{p\_id}[-K_{p\_vd}(v_{Cq0} + R_v i_{Lq0} + \omega_1 L_v i_{Ld0}) + \omega_1 C_f v_{Cd0} - i_{Lq0}]/L_f$, $A_{2(12,6)} = (\omega_1 L_f i_{Lq0} + v_{cd0})/L_f + K_{p\_iq}[K_{p\_vq}(v_{Cd0} + R_v i_{Ld0} - \omega_1 L_v i_{Lq0}) + \omega_1 C_f v_{Cq0} + i_{Ld0}]/L_f$, $A_{2(12,7)} = -K_{p\_vd}v_{Cq0} + \omega_1 C_f v_{Cd0} - i_{Lq0} + K_{p\_vd}(-R_v i_{Lq0} - \omega_1 L_v i_{Ld0})$, $A_{2(12,8)} = K_{p\_vq}v_{Cd0} + \omega_1 C_f v_{Cq0} + i_{Ld0} + K_{p\_vq}(R_v \cdot i_{Ld0} - \omega_1 L_v i_{Lq0})$, $A_{2(12,9)} = -R_v i_{Lq0} - \omega_1 L_v i_{Ld0} - v_{Cq0}$, and $A_{2(12,10)} = R_v i_{Ld0} - \omega_1 L_v i_{Lq0} + v_{Cd0}$.

$$\mathbf{A}_{3(13\times13)} =$$

$$\begin{bmatrix}
\frac{-R_g}{L_g} & \omega_1 & \frac{1}{L_g} & 0 & 0 & 0 & 0 & 0 & 0 & 0 & 0 & 0 & 0 \\
-\omega_1 & \frac{-R_g}{L_g} & 0 & \frac{1}{L_g} & 0 & 0 & 0 & 0 & 0 & 0 & 0 & 0 & 0 \\
\frac{-1}{C_f} & 0 & 0 & \omega_1 & \frac{1}{C_f} & 0 & 0 & 0 & 0 & 0 & 0 & 0 & 0 \\
0 & \frac{-1}{C_f} & -\omega_1 & 0 & 0 & \frac{1}{C_f} & 0 & 0 & 0 & 0 & 0 & 0 & 0 \\
0 & 0 & \frac{-1}{L_f} & 0 & \frac{R_f + K_{p_id}}{-L_f} & 0 & \frac{K_{i_id}}{L_f} & 0 & \frac{K_{p_id}}{L_f} & 0 & 0 & \frac{-K_{p_id} i_{Lq0} + \omega_1 L_f i_{Ld0} - v_{cq0}}{L_f} & 0 \\
0 & 0 & 0 & \frac{-1}{L_f} & 0 & \frac{R_f + K_{p_iq}}{-L_f} & 0 & \frac{K_{i_iq}}{L_f} & 0 & \frac{K_{p_iq}}{L_f} & 0 & \frac{K_{p_iq} i_{Ld0} + \omega_1 L_f i_{Lq0} + v_{cd0}}{L_f} & 0 \\
0 & 0 & 0 & 0 & -1 & 0 & 0 & 0 & 1 & 0 & 0 & -i_{Lq0} & 0 \\
0 & 0 & 0 & 0 & 0 & -1 & 0 & 0 & 0 & 1 & 0 & i_{Ld0} & 0 \\
0 & 0 & \frac{-1}{L_v} & 0 & 0 & 0 & 0 & 0 & \frac{-R_v}{L_v} & \omega_1 & 0 & \frac{-v_{Cq0}}{L_v} & \frac{-n_q}{L_v} \\
0 & 0 & 0 & \frac{-1}{L_v} & 0 & 0 & 0 & 0 & -\omega_1 & \frac{-R_v}{L_v} & 0 & \frac{v_{Cd0}}{L_v} & 0 \\
\frac{3}{2}\omega_{LPF} v_{Cd0} & \frac{3}{2}\omega_{LPF} v_{Cq0} & \frac{3}{2}\omega_{LPF} i_{gd0} & \frac{3}{2}\omega_{LPF} i_{gq0} & 0 & 0 & 0 & 0 & 0 & 0 & -\omega_{LPF} & 0 & 0 \\
0 & 0 & 0 & 0 & 0 & 0 & 0 & 0 & 0 & 0 & -m_p & 0 & 0 \\
\frac{3}{2}\omega_{LPF} v_{Cq0} & \frac{-3}{2}\omega_{LPF} v_{Cd0} & \frac{-3}{2}\omega_{LPF} i_{gq0} & \frac{3}{2}\omega_{LPF} i_{gd0} & 0 & 0 & 0 & 0 & 0 & 0 & 0 & 0 & -\omega_{LPF}
\end{bmatrix} \tag{A3}$$

REFERENCES

[1] J. Matevosyan, B. Badrzadeh, T. Prevost, E. Quitmann, D. Ramasubramanian, et al., "Grid-forming inverters: Are they the key for high renewable penetration?," *IEEE Power Energy Mag.*, vol. 17, no. 6, pp. 89-98, Nov.-Dec. 2019.

[2] J. Rocabert, A. Luna, F. Blaabjerg and P. Rodríguez, "Control of power converters in AC microgrids," *IEEE Trans. Power Electron.*, vol. 27, no. 11, pp. 4734-4749, Nov. 2012.

[3] D. Pan, X. Wang, F. Liu and R. Shi, "Transient stability of voltage-source converters with grid-forming control: A design-oriented study," *IEEE J. Emerg. Sel. Top. Power Electron.*, vol. 8, no. 2, pp. 1019-1033, Jun. 2020.

[4] R. Rosso, X. Wang, M. Liserre, X. Lu and S. Engelken, "Grid-forming converters: control approaches, grid-synchronization, and future trends - A review," *IEEE Open J. Ind. Appl.*, vol. 2, pp. 93-109, 2021.

[5] K. De Brabandere, B. Bolsens, J. Van den Keybus, A. Woyte, J. Driesen and R. Belmans, "A voltage and frequency droop control method for parallel inverters," *IEEE Trans. Power Electron.*, vol. 22, no. 4, pp. 1107-1115, Jul. 2007.

[6] S. D'Arco and J. A. Suul, "Virtual synchronous machines - classification of implementations and analysis of equivalence to droop controllers for microgrids," *IEEE Gren. Conf.*, pp. 1-7, 2013.

[7] P. Mitra, L. Zhang and L. Harnefors, "Offshore wind integration to a weak grid by VSC-HVDC links using power-synchronization control: A case study," *IEEE Trans. Power Del.*, vol. 29, no. 1, pp. 453-461, Feb. 2014.

[8] K. Yu, Q. Ai, S. Wang, J. Ni and T. Lv, "Analysis and optimization of droop controller for microgrid system based on small-signal dynamic model," *IEEE Trans. Smart Grid*, vol. 7, no. 2, pp. 695-705, Mar. 2016.

[9] Y. Liao, X. Wang, F. Liu, K. Xin and Y. Liu, "Sub-synchronous control interaction in grid-forming VSCs with droop control," *IEEE Work. Electron. Grid (eGrid)*, pp. 1-6, 2019.

[10] W. Du, Z. Chen, K. P. Scheider, R. H. Lasseter, S. P. Nandanoori, et al., "A comparative study of two widely used grid-forming droop controls on microgrid small-signal stability," *IEEE J. Emerg. Sel. Top. Power Electron.*, vol. 8, no. 2, pp. 963-975, Jun. 2020.

[11] J. C. Vasquez, J. M. Guerrero, M. Savaghebi, J. Eloy-Garcia and R. Teodorescu, "Modeling, analysis, and design of stationary-reference-frame droop-controlled parallel three-phase voltage source inverters," *IEEE Trans. Ind. Electron.*, vol. 60, no. 4, pp. 1271-1280, Apr. 2013.

[12] P. Rodriguez, I. Candela and A. Luna, "Control of PV generation systems using the synchronous power controller," *IEEE Energy Conv. Cong. Expos. (ECCE)*, pp. 993-998, 2013.

[13] L. Huang, C. Wu, D. Zhou, and F. Blaabjerg, "A simplified SISO small-signal model for analyzing instability mechanism of grid-forming inverter under stronger grid," *IEEE Work. Contr. Model. Power Electron. (COMPEL)*, 2021, in press.

[14] L. Huang, C. Wu, D. Zhou, and F. Blaabjerg, "Impact of grid strength and impedance characteristics on the maximum power transfer capability of grid-connected inverters," *Appl. Sci.*, vol. 11, no. 9, p. 4288, May 2021.

[15] L. Huang, C. Wu, D. Zhou, and F. Blaabjerg, "A double-PLLs-based impedance reshaping method for extending the stability range of grid-following inverter under weak grid," *IEEE Trans. Power Electron.*, 2021, conditional acceptance.

[16] L. Huang, C. Wu, D. Zhou, and F. Blaabjerg, "Comparison of three small-signal stability analysis methods for grid-following inverter," *Int. Conf. Opt. Electr. Electron. Equip. (OPTIM)*, 2021, in press.